An extended DNA-free intranuclear compartment organizes centrosomal microtubules in Plasmodium falciparum

Caroline S. Simon[1], Yannik Voß[1], Charlotta Funaya[2], Marta Machado[1,3], Alexander Penning[1], Darius Klaschka[1], Marek Cyrklaff[1], Juyeop Kim[1], Markus Ganter[1], Julien Guizetti[1*]

[1] Centre for Infectious Diseases, Heidelberg University Hospital, Heidelberg, Germany
[2] Electron Microscopy Core Facility, Heidelberg University, Heidelberg, Germany
[3] Graduate Program in Areas of Basic and Applied Biology, Instituto de Ciências Biomédicas Abel Salazar, Porto University, Porto, Portugal.

*correspondence: julien.guizetti@med.uni-heidelberg.de

Keywords

Malaria, Mitosis, Cell division, MTOC, Centrosome, Microtubule, Centrin, Super-resolution, Electron tomography

Abstract

Rapid proliferation of *Plasmodium falciparum* parasites in human red blood cells is the cause of malaria and is underpinned by an unconventional cell division mode, called schizogony. Contrary to model organisms, *P. falciparum* replicates by multiple rounds of closed and asynchronous nuclear divisions that are not interrupted by cytokinesis. Organization and dynamics of the critical nuclear division factors are, however, poorly understood. Centriolar plaques, the centrosomes of *P. falciparum*, are important regulators of division and serve as microtubule organizing centers. Early microscopy studies reveal an acentriolar, amorphous structure although its detailed organization remains elusive. Intranuclear microtubules mediate chromosome segregation, but the small size of parasite nuclei has precluded detailed analysis of their arrangement by classical fluorescence microscopy. We apply our recently developed STED super-resolution microscopy protocol and live cell imaging to describe the reconfiguration of microtubules during schizogony. Analysis of centrin, nuclear pore, and microtubule positioning reveals a bipartite organization of the centriolar plaque. While centrin is extranuclear, we confirm by correlative light and electron tomography that microtubules are nucleated in a previously unknown and extended intranuclear compartment, which is devoid of chromatin. This study enables us to build a working model of the organization of an unconventional centrosome and better understand the diversity of eukaryotic cell division modes.

Introduction

Plasmodium falciparum encounters significant population bottlenecks when being transmitted between humans and mosquitoes. To overcome those it undergoes several phases of extensive proliferation. When a mosquito takes up an infected blood meal a rapid series of division events is triggered resulting in the formation of eight male gametes from a single gametocyte within only 15 minutes (Fang et al., 2017; Sinden et al., 1978). During the subsequent oocyst stage at the mosquito midgut thousands of sporozoites are produced of which very few reach the human liver after an infectious mosquito bite (Beier, 1998; Vaughan, 2007). Once those sporozoites invade a hepatocyte they can generate more than ten thousand daughter cells within one cycle, which are then released into the blood (Prudêncio et al., 2006; Sturm et al., 2006). There, repeated rounds of red blood cell invasion, growth, division, and egress cause the high parasite loads, which lead to all clinical symptoms associated with malaria (Schofield, 2007). The cell division processes that underlie these unconventional proliferation events are, however, poorly understood (Francia and Striepen, 2014; Gubbels et al., 2020; Matthews et al., 2018).

Successful division requires a series of cellular events. Chromosomes must be replicated alongside duplication of the centrosomes, which act as the poles towards which sister chromatids are segregated. Thereafter nuclei are physically separated and the cytoplasm is divided by cytokinesis. *P. falciparum*, however, uses an unconventional division mode, called schizogony where several rounds of nuclear divisions are not interrupted by cytokinesis, which leads to formation of multinucleated parasite stages (Leete and Rubin, 1996). Although nuclei share a common cytoplasm in schizonts nuclear divisions are asynchronous (Arnot et al., 2011; Dorin-Semblat et al., 2011; Read et al., 1993). Throughout nuclear division the nuclear envelope remains intact and the DNA is not condensed (Read et al., 1993). Once all rounds of nuclear division are completed each of the 8-28 nuclei are packaged into individual daughter cells, called merozoites (Garg et al., 2015; Reilly et al., 2007). Upon rupture of the infected host cell, merozoites are released and invade new red blood cells.

Centrosomes are generally regarded as key regulatory hubs of the cell cycle and their duplication limits the number of nuclear divisions (Fu et al., 2015). The centrosome of *P. falciparum* is called centriolar plaque. It exhibits important morphological differences when compared to model organisms such as vertebrate centrosomes or the spindle pole bodies in yeast (Rüthnick and Schiebel, 2018). Available data on the organization of the centriolar plaque is very limited. In early transmission electron microscopy studies, mainly done in oocysts in the mosquito midgut, centriolar plaques appear as electron-dense areas that neither show centrioles nor any other distinct structures (Aikawa & Beaudoin, 1968; Aikawa, Huff, & Sprinz, 1967; Canning & Sinden, 1973; Howells & Davies, 1971; Schrével, Asfaux-Foucher, & Bafort, 1977; Sinden, Canning, & Spain, 1976; Terzakis, Sprinz, & Ward, 1967). Centriolar plaques seem partially embedded in the nuclear membrane, but their positioning relative to the nuclear pore-like “fenestra” remains unclear. Generally, the amorphous appearance of centriolar plaques in electron microscopy has precluded a detailed analysis of their organization so far. The centrosome of a related apicomplexan parasite *Toxoplasma gondii,* which does contain centrioles, shows a bipartite organization with a distinct inner and outer core (Suvorova et al., 2015). Further, few canonical centrosome components are conserved in *Plasmodium* with the exception of centrins, a family of small calcium binding proteins implicated in centrosome duplication (Azimzadeh and Bornens, 2007; Mahajan et al., 2008; Roques et al., 2019), and the microtubule nucleating complex around gamma-tubulin (Zupa et al., 2020). Before we begin to understand the

82 regulation of centriolar plaque duplication and nuclear division we must know the arrangement and
83 dynamics of key division factors around this atypical centrosome.
84
85 Centriolar plaques act as microtubule organizing centers. During schizogony intranuclear
86 microtubules organization is very heterogeneous and several atypical structures such as plaques,
87 hemispindles, and the particularly small mitotic spindles have been described (Arnot et al., 2011;
88 Fennell et al., 2006, 2008; Read et al., 1993). Tubulin-rich plaques were equated with the centriolar
89 plaques, but their size clearly exceeds the dimensions of electron dense regions described in electron
90 microscopy studies (Gerald et al., 2011). Hemispindles were often interpreted as half-spindles, that
91 form a bipolar mitotic spindle by fusion (Fennell et al., 2006, 2008; Read et al., 1993; Schrével et al.,
92 1977). Inconsistencies in the observed size bring fusion of hemispindles during schizogony into
93 question. While hemispindles observed in electron microscopy are about 0.5 to 0.7 µm in length,
94 which is more consistent with an early stage of a mitotic spindle, hemispindles described by tubulin
95 antibody staining are extensive structures measuring around 2-4 µm. In another study, hemispindles
96 observed in oocysts were interpreted as post-anaphase spindles (Canning and Sinden, 1973). These
97 data provide a controversial view on the occurrence, dynamics, and function of hemispindles, which
98 needs to be clarified. We have recently established STED nanoscopy for blood stages, which allowed
99 us to resolve distinct microtubule nucleation sites (Mehnert et al., 2019). These findings were
100 recently confirmed by expansion microscopy (Bertiaux et al., 2021; Guizetti and Frischknecht, 2021).
101 Where microtubule nucleation sites are positioned relative to the nuclear envelope is still an open
102 question.
103
104 In this study we use a combination of super-resolution, live cell, and electron microscopy to reveal
105 the ultrastructural organization of the centriolar plaque and microtubules in dividing *P. falciparum*
106 blood stage parasites. We characterize their unconventional dynamics and reveal a novel subnuclear
107 compartment that harbors microtubule nucleation sites and is devoid of chromatin.
108
109 **Results**
110
111 To analyze centriolar plaque and microtubule dynamics we carried out time-lapse imaging of the first
112 nuclear divisions in a blood stage *P. falciparum* parasite strain that episomally expresses PfCentrin1-
113 GFP and was labeled with SPY555-Tubulin, a live cell compatible microtubule dye (Wang et al., 2020).
114 To reduce phototoxicity we applied gentle illumination conditions and used HyVolution-based image
115 processing to generate sufficient image contrast to detect those weak signals. Initially, microtubules
116 dynamically extended from the centriolar plaque forming hemispindle structures (Fig. 1A). This was
117 followed by a prolonged phase, where the tubulin signal accumulated close to the PfCentrin1-GFP
118 signal. Finally, the tubulin signal elongated while the distance between centrin foci increased, which
119 likely corresponded to anaphase. We quantified the mean duration of hemispindle, accumulation,
120 and anaphase stages throughout the first three nuclear divisions (Fig. 1B). Every microtubule
121 organization stage was significantly longer in the first division when compared to the second or third
122 (Fig. S1A). The precise time point of initial appearance of the centrin focus was sometimes difficult to
123 determine and also depended on PfCentrin1-GFP expression levels (Fig. 1C). In cells with a stronger
124 signal appearance of the centrin focus already coincided with the hemispindle microtubule stage (Fig.
125 1A). In more weakly expressing cells it was only detectable later or sometimes not at all. A second
126 centrin focus appeared about 65 min on average after the first one (Fig. S1B). This was promptly

127 followed by anaphase indicating that a mitotic spindle was assembled during centrin signal
128 duplication. The now segregated centrin foci were again associated with dynamic hemispindle
129 structures, which subsequently went through a collapsed stage prior to initiating the next duplication
130 and elongation event. Frequently, the second and third round of spindle elongation occurred in an
131 asynchronous fashion.
132
133 Due to the inherent resolution and sensitivity limits of live cell imaging we could not precisely
134 determine the appearance of the centrin signal and its duplication. Further, we wanted to analyze
135 organization of endogenous centrin and its exact positioning relative to microtubules. Therefore, we
136 imaged parasites at different stages of schizogony after immunolabeling with anti-tubulin and anti-
137 centrin antibodies by dual-color STED nanoscopy. While ring and early trophozoite stage parasites do
138 not express tubulin or centrin (Fig. S2), we identified hemispindle structures already in
139 mononucleated late trophozoites (Fig. 1D). Consistent with our live cell imaging data, only some of
140 the hemispindles were associated with a centrin signal before the first division, while afterwards
141 every nucleus was accompanied by one or two centrin foci. The collapse of hemispindles into an
142 intense and compact tubulin accumulation is associated with duplication of the centrin foci. At which
143 point tubulin is reorganized into the bipolar microtubule array, which then forms the mitotic spindle
144 cannot be resolved here. However, early stages where duplicated centrin foci are proximal can be
145 differentiated from late stages where they oppose each other with DNA in the middle. Occasionally,
146 two nuclei connected by an elongated microtubule structure, which we interpret as anaphase
147 spindles, can be observed. In multinucleated stages, several different microtubule organizations
148 could be observed simultaneously, reflecting the asynchrony of nuclear divisions. Cytokinetic
149 segmenter stages on the other hand lack distinct centrin foci and intranuclear microtubules, but
150 clearly display the microtubule cytoskeleton associated with the inner membrane complex.
151
152 Since the role of hemispindles is unclear we wanted to test whether they might be involved in
153 recruitment of centromeres, akin to a “search-and-capture” mechanism (Heald and Khodjakov,
154 2015), which could assist their clustering at the nuclear periphery (Hoeijmakers et al., 2012).
155 Therefore, we co-labeled tubulin with an anti-CenH3 antibody, which specifically marks centromeric
156 histones (Fig. 1E). As expected, the centromere signal clustered at the periphery next to the
157 centriolar plaque (Zeeshan et al., 2020). However, STED nanoscopy reveals that CenH3 foci were
158 virtually always distinct from hemispindle microtubules, precluding any direct interaction at the
159 acquired time points.
160

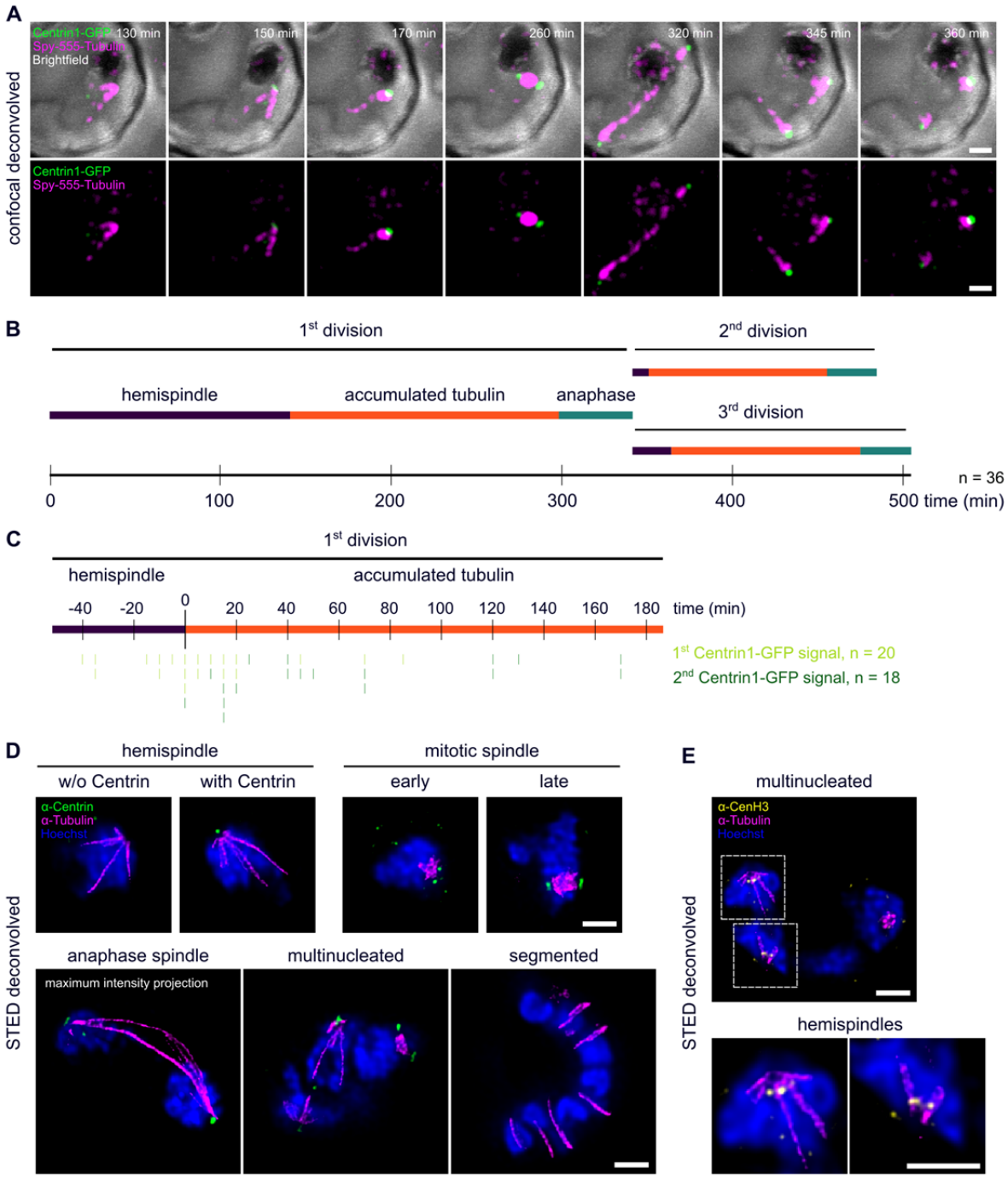

Figure 1) Live cell and super-resolution microscopy of microtubule, centriolar plaque, and centromere reorganization throughout schizogony. *A) Deconvolved confocal time-lapse microscopy still images of first spindle formation and elongation in a schizont ectopically expressing PfCentrin1-GFP (green) and labeled with SPY555-Tubulin (magenta). Maximum intensity projections are shown. B) Quantification of mean duration of three distinct microtubule organization phases in 36 movies. Since most movies (32/36) were already started during hemispindle phase we could only quantify the minimal mean length of hemispindle stage for the first division. C) Time points of appearance of first and second clear PfCentrin1-GFP signal normalized to the start of accumulated tubulin phase. D) Dual-color STED nanoscopy images of different schizogony stages of parasites labeled with anti-centrin (green), anti-tubulin (magenta) antibodies and stained with Hoechst (blue). Single slices are shown except for the anaphase spindle. E) like D) with anti-tubulin (magenta) and anti-CenH3 (yellow) showing centromere positioning. All scale bars are 1 µm.*

175 Notably, all images revealed a significant gap between centrin and tubulin signals (Fig. 1D). The
176 question whether microtubules and centrin locate inside or outside the nucleus remains open. In
177 absence of a known nuclear envelope marker for *Plasmodium* spp., we used a strain where the
178 nuclear pore protein Nup313 has been tagged endogenously with 3xHA (Fig. S3) to partly mark the
179 nuclear boundary (Kehrer et al., 2018). Immunofluorescence co-staining with centrin and tubulin
180 revealed that centrin signals localize on the cytoplasmic side, while microtubule ends are localized
181 inside the nucleus during all stages of schizogony (Fig. 2A). We, also, consistently observed a
182 Hoechst-free region right beneath the centrin foci, which has not been described previously. In nuclei
183 with accumulated tubulin signals those localize within this region. To test if this region is indeed
184 devoid of DNA and not a result of inefficient Hoechst labeling we stained cells with DRAQ5, which is
185 an intercalating DNA dye not sensitive to heterochromatin state (Fig. 2B). This staining confirmed the
186 absence of DNA from this region beneath centrin. To further assess the position of the nuclear
187 boundary at the centriolar plaque we used a strain ectopically expressing mCherry tagged with three
188 nuclear localization signals (NLS) to stain the nucleoplasm (Fig. 2B). The NLS-mCherry signal was
189 overlapping with the DNA-free region suggesting that there is an extended subnuclear compartment
190 devoid of DNA associated with the centriolar plaque.
191
192 To more directly visualize the nuclear membrane and the ultrastructural features surrounding the
193 centriolar plaque we used electron microscopy (EM). Initial analysis of schizont nuclei with
194 transmission EM suggested that an intranuclear region associated with microtubules is, indeed,
195 delineated by a non-membranous boundary (Fig. S4). However, due to their amorphous structure
196 centriolar plaques cannot be consistently identified in those electron microscopy samples. Hence, we
197 adapted an in-resin correlative light and electron microscopy (CLEM) approach (Kukulski et al., 2012)
198 to our system using the PfCentrin1-GFP expressing parasite line. In addition, we labeled the cells with
199 the infrared DNA dye 5-SiR-Hoechst (Bucevičius et al., 2019). The fluorescent signal was preserved in
200 the samples prepared for electron microscopy and resin sections were imaged on a widefield
201 fluorescence microscope to identify the residual PfCentrin1-GFP foci (Fig. 2C). Using overview images
202 and finder grids we were able to relocate individual cells at the electron microscope. Overlaying the
203 fluorescence image with the electron tomogram allowed us to unambiguously define the centriolar
204 plaque position. 5-SiR-Hoechst signal was also still detectable after sample preparation but, likely due
205 to imaging a limited section of the nucleus, the staining was not uniform and mostly limited to
206 electron dense heterochromatin regions. We could not detect any invagination of the nuclear
207 membrane adjacent to the centrin signal. We, however, identified an underlying region with distinct
208 electron density distribution, which was sometimes associated with microtubules (Fig. 2C). The size
209 and shape of that region corresponded well to the Hoechst-free region observed in our
210 immunofluorescence staining suggesting that this is, indeed, a novel intranuclear compartment with
211 centrosomal function.
212

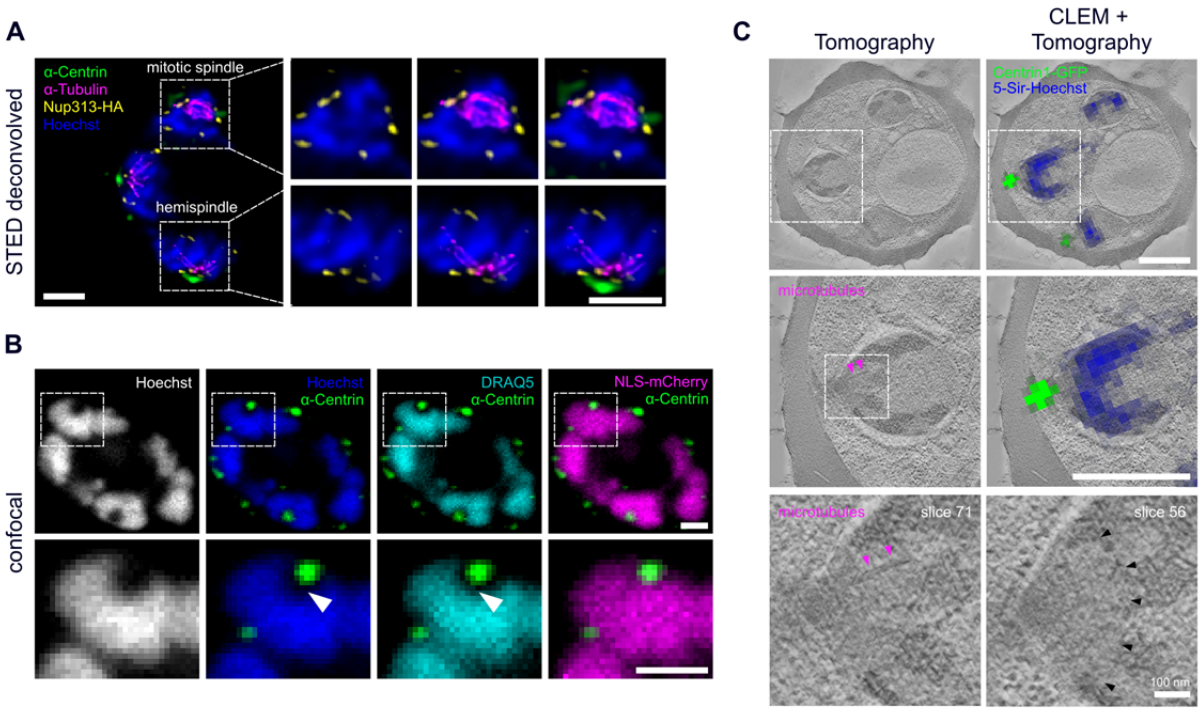

Figure 2) Centriolar plaques are divided in an extranuclear centrin-containing compartment and an intranuclear DNA-free compartment associated with microtubules. *A) Dual-color STED nanoscopy images of schizont strain expressing HA-tagged nuclear pore protein Nup313-HA (yellow) labeled with anti-HA and anti-tubulin (magenta) overlayed with confocal images of anti-centrin (green) and Hoechst-staining (blue). B) Confocal images of schizont ectopically expressing NLS-mCherry (magenta) labeled with anti-centrin (green) and stained for DNA with Hoechst (blue) and DRAQ5 (turquoise). C) Correlative in-resin widefield fluorescence and electron tomography images of thick sections of a high-pressure frozen and embedded schizont expressing PfCentrin1-GFP (green) and stained for DNA with 5-SiR-Hoechst (blue). Same cell region containing clear PfCentrin1-GFP foci was imaged by fluorescence microscopy and overlayed with an electron tomography slice. In zoom ins arrows indicate microtubule (magenta) and boundary-like region (black) for two image slices. All scale bars are 1µm, except were indicated.*

Due to difficulties using UV for resin polymerization in the pigmented erythrocytes we also tried embedding in a resin, LR gold, which can be polymerized chemically and these samples were used for the CLEM approach. Still the samples retrieved from UV polymerized HM20 showed superior contrast and were used for investigating more details of the microtubule organization in nuclei of the schizont stage by electron tomography. We found nuclear stages containing highly elongated individual microtubules which can deform the nuclear envelope at their tips and likely correspond to hemispindles (Fig. 3A). Here, the resolution was sufficient to distinctly identify the characteristically shaped microtubule nucleation complex around gamma-tubulin, which demarcates microtubule minus ends. Those were emerging from discrete positions underlying an electron dense region at the nuclear envelope. A distinct intranuclear compartment could, however, only be surmised in some nuclei when using this sample preparation method (Fig. S5). Mitotic spindles displayed a short but much denser array of microtubules with minus ends clustered at a substantial distance from the nuclear envelope (Fig. 3B). Taken together these data suggest that intranuclear microtubule nucleation sites are embedded inside an extended amorphous matrix rather than linked to a membrane-associated centrosomal protein complex.

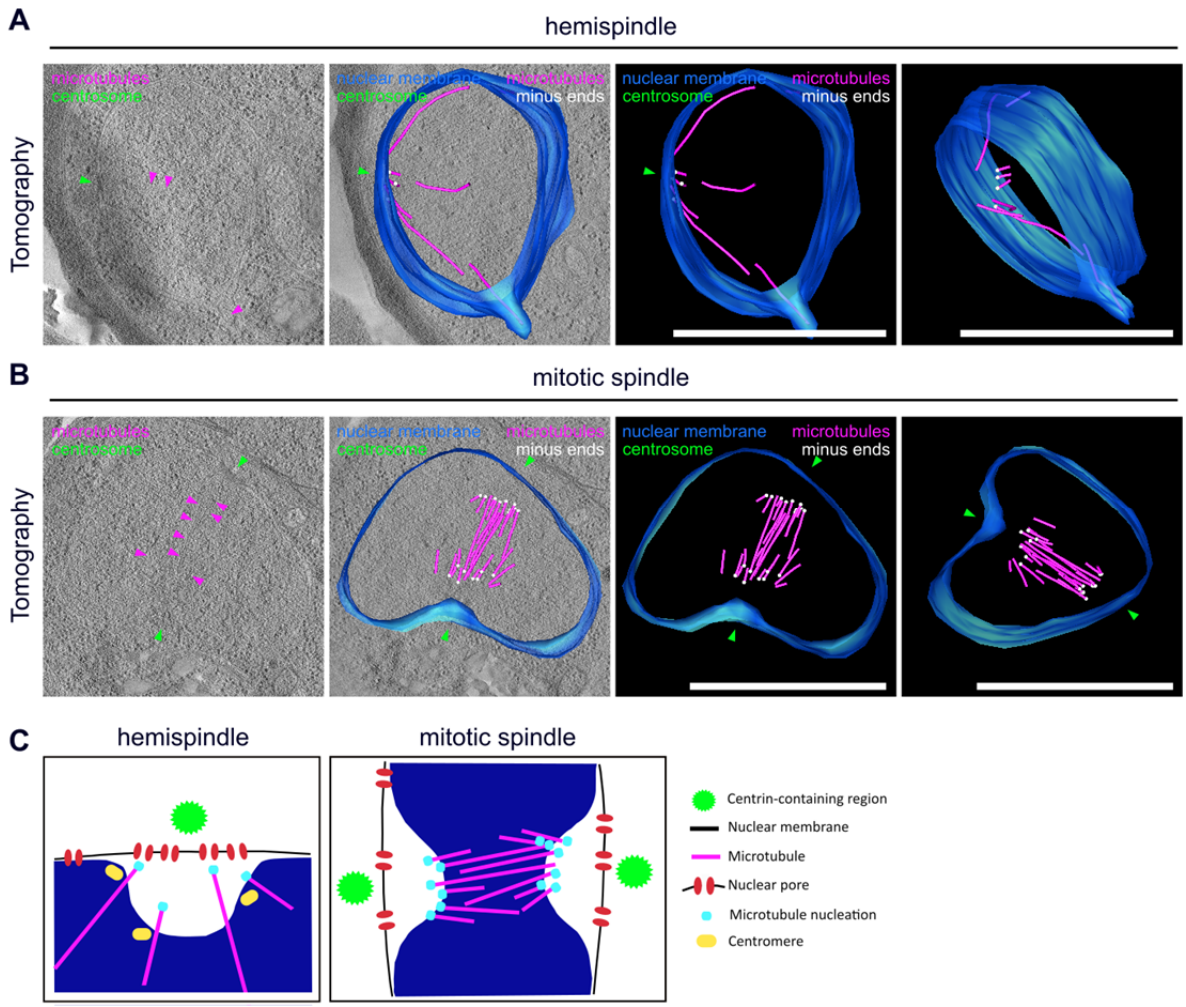

Figure 3) Centriolar plaque microtubule nucleation sites are distinct and detached from a defined nuclear membrane associated complex. *A) 3D electron tomograms of thick-sections (200nm) of schizont nucleus in hemispindle stage. Corresponding surface rendering of microtubules (magenta), nuclear membrane (blue), microtubule minus ends (white), and likely position of centriolar plaques (green) are shown. B) as A) for mitotic spindle stage. All scale bars are 1 µm. C) Schematic model of centriolar plaque organization during hemispindle and mitotic spindle stages in blood stage schizonts. Content of the DNA-free intranuclear region harboring microtubule nucleation sites is unknown.*

Discussion

Our data provide an entirely novel perspective on the organization of the centriolar plaque and significantly expands on previous concepts depicting it merely as an electron-dense zone, which is inserted in the nuclear membrane (Prensier and Slomianny, 1986). This study highlights the significant differences to the well-characterized spindle pole bodies in budding yeast, where intranuclear microtubules emanate from a small and spatial well-defined protein complex which extends into the cytoplasm (Kilmartin, 2014). We reveal a bipartite organization of the centriolar plaque with an extranuclear region containing centrin and an intranuclear region harboring microtubule nucleation sites (Fig. 3C). While this seems to some degree reminiscent of the inner and outer core described for the centrosome in *T. gondii* (Suvorova et al., 2015), we note important differences. In *T. gondii,* centrin has been localized to the inner core and it has been indicated that both cores are extranuclear (White and Suvorova, 2018). They are likely separated by the prominent

264 additional membrane layer that characterizes the centrocone, but is absent from centriolar plaques.
265 Due to the consistent presence of nuclear pores at the centriolar plaque it is plausible that they are
266 involved in linking the intra- and extranuclear compartments. Whether some of those pores are
267 remodeled to constitute more "fenestra-like" structures remains to be investigated (Bannister et al.,
268 2000).
269
270 We further clarify microtubule dynamics, which underlie their heterogeneous organization,
271 previously described in fixed cells (Arnot et al., 2011; Fennell et al., 2006, 2008; Read et al., 1993).
272 Hemispindles are already present early in mononucleated cells indicating that they are not per se
273 post-anaphase remnants as suggested earlier (Canning and Sinden, 1973). Their function, however,
274 remains elusive. We could abate the conspicuous hypothesis that they are directly involved in
275 clustering centromeres at the nuclear periphery, which is consistent with findings in yeast where
276 perinuclear centromere clustering has already been shown to be microtubule-independent
277 (Richmond et al., 2013). An alternative explanation for the presence of hemispindles is that once
278 tubulin accumulates beyond the required critical concentration microtubules polymerize
279 spontaneously (Walker et al., 1988). After the hemispindle stage the tubulin signal collapses into a
280 smaller focus, which is akin to the "tubulin rich plaques" (Gerald et al., 2011). The increased
281 sensitivity and resolution of our assays, however, demonstrate that tubulin accumulations are
282 virtually always associated with two centrin signals raising the hypothesis that those structures are
283 early mitotic spindles. When and to which extent microtubules are polymerized into structured
284 bipolar spindles is not resolved, but we can at this point exclude that they are the result of fusion
285 between hemispindles, as previously suggested (Gerald et al., 2011). This early centriolar plaque
286 duplication might be associated with S-phase onset as hypothesized earlier (Francia and Striepen,
287 2014).
288
289 Lastly, we did not observe intranuclear microtubules to be in contact with the nuclear membrane or
290 membrane-associated structures, like for spindle pole bodies (Kilmartin, 2014). Rather, microtubules
291 are nucleated from distinct sites within an extended nuclear compartment which is free of chromatin
292 and has not been described before. Despite the absence of centrioles, the preservation of the
293 nuclear membrane, and the lack of conserved factors this structure is vaguely reminiscent of the
294 pericentriolar material, which makes up the outer layer of vertebrate centrosomes and harbors
295 microtubule nucleation complexes (Woodruff et al., 2014). Deciphering the composition of this novel
296 nuclear compartment, understanding how it is assembled, and how it splits are some of the more
297 pressing questions emerging from this study.
298

299 Materials and Methods

300

301 Parasite culture

302 *Plasmodium falciparum* cell lines NF54_Centrin1-GFP and 3D7_Nup313-HA_glms were cultured in O+
303 human red blood cells in RPMI 1640 medium supplemented with 0.2 mM hypoxanthine, 25mM
304 HEPES, 0.5% Albumax and 12.5 µg/ml Gentamicin. Cultures were maintained at a hematocrit of
305 about 3% and a parasitemia of 3-5%. Parasite cultures were incubated at 37°C with 90% humidity, 5%
306 O_2 and 3% CO_2. To synchronize cultures, late stage parasites were lysed by 5% sorbitol treatment.
307

308 Plasmid constructs

309 To generate a pArl-Centrin1-GFP plasmid for episomal expression of PfCentrin1-GFP in NF54, we used
310 a pArl-PfCentrin3-GFP plasmid (kindly provided by Tim Gilberger). The pArl-PfCentrin3-GFP plasmid
311 was digested with KpnI-HF and AvRII to cut out the PfCentrin3. The PfCentrin1 insert sequence was
312 generated from *P. falciparum* cDNA via PCR using the forward primer
313 CGACCCGGGATGGTACCATGAGCAGAAAAAATCAAACTATG and reverse primer
314 TTCTTCTCCTTTACTCCTAGGAAATAAGTTGGTCTTTTTCATAATTC. PfCentrin1 and the digested backbone
315 were ligated using Gibson Assembly and the sequence was verified by Sanger sequencing. To
316 generate the pSLI-Nup313-3xHA_glms construct, first both HA and glmS sequences were ligated into
317 pSLI-TGD, a kind gift of Tobias Spielmann (Birnbaum et al., 2017), to obtain the pSLI-3xHA-glmS. The
318 glmS ribozyme was amplified from plasmid pARL_glmS (a kind gift from Jude Przyborski) and inserted
319 by Gibson assembly into pSLI-TGD, downstream of the NeoR/KanR resistant cassette, using primers
320 0079 and 0082. For the 3xHA tagging its sequence was first PCR-amplified with primers 0126 and
321 0127 from pDC2-cam-coCas9-U6.2-hDHFR (a kind gift from Markus Lee) and cloned by Gibson
322 assembly into NotI and MluI digested pSLI-glmS plasmid. Lastly, 757bp of NUP313 genomic sequence
323 (without stop codon) was PCR amplified using primers 0163for and 0164rev and cloned into the
324 modified pSLI-3xHA-glmS plasmid using NotI and Mlu1 restriction sites. The p3-NLS-L3-mCherry
325 construct was obtained from the p3-NLS-FRB-mCherry plasmid, a kind gift of Tobias Spielmann
326 (Birnbaum et al., 2017), by removing the FRB domain with NheI and KpnI digestion and consecutive
327 ligation. Correct sequence of inserts was verified by Sanger sequencing with following primers:
328 0160for: CGACCCGGGATGGTACCATGAGCAGAAAAAATCAAACTATG
329 0161rev: TTCTTCTCCTTTACTCCTAGGAAATAAGTTGGTCTTTTTCATAATTC
330 0079for: CGCAGCGCATCGCCTTCTATCGCCTTCTTGACGAGTTCTTCTAACTCGAGTAATTATAGCGCCCGAACTAAGCG
331 0080rev: GGTATAAATATATAAATAAGAAAAACGAACATTAAGCTGCCATATCCC
332 0126for:CCTTAGCTCATTCAGGTTTTTGTTTCGAAAAAATTATTACACCTGTGACGCGTTATCCATACGATGTTCCTGATTAT
333 GC
334 0127rev:GGATTTTCTTCTACATCTCCACATGTTAATAAACTTCCTCTTCCTTCTCCGTCGACAGCGTAATCAGGTACATCGTA
335 TGGATAAGAACC
336 0163for: ATAAGAATgcggccgcTAATGGATGTAATAAAAGTGATGATAGC
337 0164rev: CGacgcgtATTTATCATATTTTGATTCATAAATTTATGCC
338
339 **Parasite transfection**
340 Transgenic parasites were generated by electroporation of sorbitol-synchronized ring-stage parasites
341 with 50-100 µg of purified plasmid DNA (Qiagen). To select for the plasmids PArl-PfCentrin1-GFP and
342 p3-NLS-L3-mCherry, we used 2.5 nM WR99210 (Jacobus Pharmaceuticals) or 5 µg/ml blasticidin S
343 (InVivoGen), respectively. To select for integration of the Nup313-HA_glms construct into the
344 genome, we followed the protocol described previously (Birnbaum et al., 2017), using 800ug/ml
345 Geneticin-G418 (Thermo Fisher Scientific). PCRs across the integration junctions and testing for
346 leftover unmodified locus to exclude the presence of wild type were performed (Fig. S3). Limiting
347 dilution was done to obtain clonal parasite lines.
348
349 **Seeding of infected red blood cells on imaging dishes**
350 For live cell imaging, cells were seeded on round imaging dishes with glass bottom (µ-Dish 35 mm,
351 ibidi), for immunofluorescence stainings on 8-well chambered glass slides (µ-Slide 8 Well, ibidi) as
352 described previously (Gruring et al., 2011; Mehnert et al., 2019). Briefly, the glass surface was coated
353 with Concanavalin A (Sigma, 5 mg/ml in water) for 20-30min at 37°C. Dishes were rinsed twice with

354 prewarmed incomplete RPMI 1640 medium lacking Albumax and hypoxanthine. The respective
355 amount of parasite ring culture (500 µl for 35mm dishes, 150µl for each well of 8-well glass slides)
356 was washed twice with incomplete medium by centrifugation (1000g, 30sec), before addition of the
357 cells onto the glass. Cells were allowed to settle for 10min in the incubator at 37°C. By gentle shaking
358 and washing of the glass slides with prewarmed incomplete medium, unbound cells were removed
359 until a monolayer of red blood cells remained on the glass surface. Incomplete medium was replaced
360 by complete medium (4 ml for 35mm dishes, 200 µl for each well of 8-well glass slides) and cells were
361 maintained in the incubator until they were prepared for live cell imaging or fixed for
362 immunofluorescence staining.
363
364 **Immunofluorescence assay**
365 Immunofluorescence staining for confocal and STED microscopy was performed as described
366 previously (Mehnert et al., 2019). Briefly, after seeding cells at ring stage, parasites were fixed in
367 schizont stages with prewarmed 4% PFA/PBS for 20min at 37°C. PFA was washed off twice with PBS.
368 Fixed cells were either stored in PBS at 4°C for later immunofluorescence staining, or stained
369 immediately. First, cells were permeabilized with 0.1% Triton X-100/PBS for 15min at room
370 temperature and rinsed three times with PBS. To quench free aldehyde groups, cells were incubated
371 with freshly prepared 0.1 mg/ml NaBH4/PBS solution for 10min at room temperature. Cells were
372 rinsed thrice with PBS and blocked with 3% BSA/PBS for 30min. In the meantime, primary antibodies
373 were diluted in 3% BSA/PBS and centrifuged at 14.800 rpm for 10 min at 4°C to remove potential
374 aggregates. Cells were incubated with primary antibodies (see below) for 2h at room temperature.
375 Next, cells were washed three times with 0.5% Tween-20/PBS. Incubation with secondary antibodies
376 (see below) plus Hoechst in 3% BSA/PBS was performed for 1h preceding removal of aggregates as
377 described for primary antibodies. After washing twice with 0.5% Tween-20/PBS and once with PBS,
378 cells were stored in PBS at 4°C in the dark until imaging. For longer storage, antibodies were
379 occasionally fixed after staining with 4% PFA/PBS for 10-15min at room temperature. After washing
380 the cells thrice with PBS, they were likewise stored in PBS at 4°C in the dark.
381
382 **Antibodies**
383 To stain microtubules the mouse anti-alpha-tubulin B-5-1-2 was used at 1:500 (Sigma, T5168).
384 Polyclonal rabbit anti-TgCentrin1 (Fig. 2B) antibody was a kind gift of Marc-Jan Gubbels and applied
385 at 1:2000. Polyclonal rabbit anti-CenH3 antibody was a kind gift of Alan Cowman and applied at
386 1:200 (Volz et al., 2010). Rat anti-HA 3F10 (Sigma) was applied at 1:500. To generate a polyclonal
387 rabbit anti-PfCentrin3 antibody a codon-optimized sequence of PfCentrin3 (PF3D7_1027700.1) was
388 synthesized (ThermoFisher, GeneArt Strings), and cloned into the pZE13d vector (Lutz and Bujard,
389 1997) with a N-terminal 6His tag via Gibson assembly (Hifi DNA Assembly, NEB) using ClaI and PstI
390 restriction sites. The construct was transformed into chemically competent W3110Z1 E.coli (Lutz and
391 Bujard, 1997) and colonies were inoculated in 800 ml LB-Amp expression culture, which was
392 incubated at 37°C and 130 rpm until reaching an OD600 of 0.5. After induction with 1 mM IPTG
393 incubation continued for 3 h after which harvested bacteria were lysed via sonication. The lysate was
394 cleared via centrifugation and recombinant PfCen3-6His purified from the soluble fraction using Ni-
395 NTA agarose beads (QiaGen) according to the manufacturer's recommendations. The buffer was
396 exchanged to PBS via overnight dialysis and the protein further purified using the Superdex 75
397 10/300 size exclusion column (Cytiva). The final protein was used for a 63-day rabbit immunization

398 regimen and affinity purification of the resulting serum performed by Davids-Biotechnology,
399 Regensburg. The secondary antibodies used for STED, namely anti-mouse-STAR580 (Abberior), anti-
400 rabbit-Atto647 (Sigma), anti-rabbit-Atto594 (Sigma), anti-mouse-Atto647 (Sigma) and anti-rat-
401 Atto594 (Biomol) were all used at a 1:200 dilution. The secondary antibodies anti-rabbit Alexa Fluor
402 Plus 488 (Thermo Fisher Scientific) and anti-rabbit Alexa488 (Thermo Fisher Scientific) were diluted
403 1:1000. To stain DNA, DRAQ5 (Biostatus) or Hoechst33342 (Thermo Fisher Scientific) were used (both
404 1:1000). To increase the signal of 3xNLS-mCherry (Fig. 2B), cells were incubated with RFP-Booster
405 nanobody coupled to Atto 594 (Chromotek) at a dilution of 1:200.
406
407 **Preparation of infected red blood cells for live cell imaging**
408 For live cell imaging, NF54_PfCentrin1-GFP cells were seeded on glass bottom dishes as described
409 above. Imaging medium, i.e. phenol red-free RPMI 1640 supplemented with stable Glutamine and 2
410 g/l NaHCO3 (PAN Biotech) with all other supplements as in the parasite culture medium, was added.
411 Imaging medium was equilibrated in the cell culture incubator for several hours. Immediately before
412 imaging, 9 ml of equilibrated imaging medium were supplemented with 4.5 µl (1:2000 dilution) of
413 the live microtubule dye SPY555-Tubulin (Spirochrome). Culture medium in the glass bottom dish
414 with seeded cells was replaced by 8 ml imaging medium, closed tightly without creating air bubbles,
415 and sealed completely with parafilm. The imaging dish was directly taken to the incubation chamber
416 of the microscope which was prewarmed to 37°C.
417
418 **Super-resolution confocal and STED microscopy**
419 Confocal microscopy of fixed and live cells was performed on a Leica TCS SP8 scanning confocal
420 microscope with Lightning (LNG) module. LNG enables automated adaptive deconvolution after
421 acquisition to generate super-resolution images. All images were acquired using a 63x 1.4 NA
422 objective, GaAsP hybrid detectors and spectral emission filters. For live cell imaging, the adaptive
423 lightning acquisition mode was used with a pinhole of 1.2 airy units resulting in a pixel size of 53.8 nm
424 and a total image size of 18.45 x 18.45 µm (344 x 344 pixels). The pixel dwell time was 488ns. Every
425 5min, a z-stack was taken of each cell with a total size of 6 µm and an z-interval of 0.5 µm. Centrin1-
426 GFP was excited with a 488nm laser at a laser power of 0.5%, SPY555-Tubulin was excited with a
427 561nm laser with a laser power of 2%. Cells were imaged over night for a maximum of 13h. For
428 confocal imaging of fixed cells, the LNG mode was turned off and cells were acquired using a pinhole
429 of 1 airy unit and a pixel size of 72.6 nm and a total image size of 9.3 x 9.3 µm (128 x 128 pixels). The
430 pixel dwell time was 488ns. Z-stacks of 6.27 µm were acquired with an z-interval of 0.3 µm.
431 RescueSTED microscopy was performed on a single-point scanning STED/RESOLFT super resolution
432 microscope (Abberior Instruments GmbH), equipped with a pulsed 775 nm STED depletion laser and
433 three avalanche photodiodes for detection. Super-resolution images were acquired with a 100x
434 1.4NA objective, a pixel size of 20 nm and a pixel dwell time of 10 µs. The STED laser power was set
435 to 10-20%, while the other lasers (488, 594 and 640) were adjusted to the antibody combinations
436 used. To prevent destruction of hemozoin-containing cells by the high-intensity STED laser, intensity
437 thresholds (CONF levels) were defined, which needed to be reached in a confocal image before
438 automatic activation of the STED laser (adaptive illumination). CONF levels varied between 10 and
439 110 and were adjusted individually for every cell. To acquire z-stacks (anaphase spindle in figure 1B),
440 a total z-stack of 3.9 µm was acquired using a z-step size of 300nm.
441

442 **Image analysis**
443 Images were analyzed using Fiji (Schindelin et al., 2012). Quantification of time-lapse images was
444 performed on images after LNG adaptive deconvolution. Therefore, cells were examined manually to
445 determine the changes of individual tubulin stages over time as well as the first stable appearance of
446 the centrin signal. All images shown were deconvolved using Huygens professional using express
447 deconvolution with the standard template.
448
449 **Preparation of infected RBCs for Electron Tomography**
450 For high pressure freezing of infected erythrocytes, a total of 2-4 ml packed red blood cells of the
451 NF54_Centrin1-GFP strain were grown in 70-140 ml culture medium. At a parasitemia of 3-5% late
452 stage parasites, schizonts were purified using magnetic separation (VarioMACS™ Separator, Miltenyi
453 Biotec). Therefore, after attaching a flow resistor (G20 needle, 0.9 mm diameter, BD Microlance) to a
454 depletion column (CS column, Miltenyi Biotec), the assembled column was inserted into the
455 magnetic field and equilibrated with incomplete medium. The parasite culture was centrifuged
456 (2min, 800g), the pellet resuspended in around 8 ml of medium and loaded onto the column. After
457 several washing steps with prewarmed incomplete medium, the column was taken out of the
458 magnetic field and late-stage parasites were eluted using 15 ml prewarmed complete culture
459 medium. Importantly, schizonts were not in contact with PBS before HPF, as we have shown recently
460 that hemispindle microtubules are not detectable when parasites were fixed immediately after PBS
461 incubation (Mehnert et al., 2019). Purified schizonts were centrifuged (2min, 800g), the pellet
462 resuspended in 1.5 ml prewarmed complete medium, again pelleted (2min, 800g) and temporarily
463 stored at 37°C until high pressure freezing of the sample using Leica EM ICE (Leica Microsystems).
464 Briefly, aluminium or gold carriers (3 mm diameter, 100 or 200 µm depth) (Leica Microsystems) and
465 the respective lids were placed on hexadecene-soaked filter paper. Carriers were filled with around
466 1.5 µl of concentrated schizont pellet, and high pressure frozen with EM ice (Leica Microsystems).
467 Freeze substitution was done in a Leica EM AFS2 (Leica Microsystems). Samples were freeze
468 substituted in 0.3% uranyl acetate in dry acetone for 24h at -90°C, followed by an increase in
469 temperature from -90°C to -45°C in 9h (an increase of 5°C/h). The samples were incubated for
470 another 5h at -45°C, before they were rinsed 3 x 10 min with dry acetone at -45 °C. Acetone was
471 replaced by increasing concentrations of the Lowicryl HM20 25%, 50% and 75% HM20 in dry acetone
472 at -45°C for 2h each. Cells were incubated in 100% HM20 at -45°C, after 12h the solution was again
473 replaced by 100% HM20 and incubated for another 2h at -45°C. Next, UV light was applied for 48h at
474 -45°C, 13 h -45°C to +20°C (an increase of 5°C/h) and 48h at 20°C to polymerize HM20 and therefore
475 embed samples in the resin. The RBC pellets were not well polymerized due to the pigmentation of
476 the cells and areas with well embedded cells had to be selected to use for sectioning. Polymerized
477 samples were trimmed and sectioned on a UC7 ultramicrotome (Leica Microsystems). 200 nm-thick
478 sections were collected on Formvar-coated copper slot grids. Sections were contrasted with 3%
479 uranyl acetate and Reynold's lead citrate The sample quality was checked on a Jeol JEM-1400 80 kV
480 transmission electron microscope equipped with a 4k by 4k pixel TemCam F416 digital camera
481 (TVIPS). For image acquisition, the EM-Menu (TVIPS) software was used. For tomography, sections
482 were placed in a high-tilt holder (Model 2040; Fischione Instruments; Corporate Circle, PA) and the
483 cells were recorded on a Tecnai F20 EM (FEI, Eindhoven, The Netherlands) operating at 200kV using
484 the SerialEM software package (Mastronarde, 2005). Images were taken every degree over a ±60°
485 range on an FEI Eagle 4K x 4K CCD camera at a magnification of 19000x and a binning of 2 (pixel size

1.13 nm). The tilted images were aligned using tilt series patch tracking. The tomograms were generated using the R-weighted back-projection algorithm. To reconstruct the complete hemispindle, tomograms were collected from 3 serial sections, aligned and joined by using the eTomo graphical user interphase (Höög et al., 2007). Tomograms were displayed as slices one voxel thick, modelled, and analyzed with the IMOD software package (Kremer et al., 1996). Capped end of microtubules were identified as minus ends in accordance to earlier microtubule studies with similar preservation techniques (Gibeaux et al., 2012; Höög et al., 2007; O'Toole et al., 2003).

Correlative in-resin widefield fluorescence and electron tomography (CLEM)

For in-resin CLEM, NF54_Centrin1-GFP cells were purified using magnetic separation as described above. Before high pressure freezing, purified late stage parasites were incubated with 1 µM of the live dye 5-SiR-Hoechst for about 1h at 37°C. The HPF was performed was described above. For CLEM, the freeze substitution and embedding was done in an Automatic Freeze Substitution System (AFS2, Leica Microsystems), but pipetting steps were performed manually. Freeze substitution was done in 0.3% uranyl acetate in dry acetone for 29h at -90°C, before the temperature was increased to -45°C in 9h (an increase of 5°C/h) and kept in the freeze substitution solution for at least 5h at -45°C. The freeze substitution solution was replaced by 100% cold, dry ethanol and the temperature was increased from -45°C to -25°C in 1h (an increase of 20°C/h). Ethanol was replaced by increasing concentrations of the resin LRGold (London Resin company). Samples were incubated with 25%, 50% and 75% LRGold in dry ethanol at -25°C for 2h each. Afterwards, 100% LRGold was added, removed and again added for overnight incubation of the samples with the resin at -25°C. The resin LRGold was supplemented with the initiator, 1.5% benzoyl peroxide, on ice. The solution was inverted carefully to prevent oxygen incorporation and immediately placed at -20° to prevent direct polymerization. Samples were incubated with 100% LRGold with initiator for 26h at -25°C. The temperature was increased from -25°C to 20°C in 9h (an increase of 5°C/h) and 24h at 20°C. Samples were trimmed with a UC7 ultramicrotome (Leica Microsystems) and 300nm-thick sections were collected on Formvar-coated finder grids to identify the position of cells in fluorescence and electron microscopy. Immediately after sectioning, the grid was slightly dried with a paper to hinder sections from moving on the grid and directly placed in a drop of PBS with pH 8.4 (Ader and Kukulski, 2017) on a glass coverslip with the sections facing the bottom. A second glass coverslip was added on top and the sandwich was mounted in a metal ring holder (Kukulski et al., 2011). Fluorescence was imaged immediately on a Zeiss Axio Observer.Z1 widefield system equipped with an AxioCam MR R3 camera and a 63x oil objective (1.4 numerical aperature). For excitation of Centrin1-GFP, a 488nm laser was used, for excitation of 5-Sir-Hoechst, a 587nm laser, both set to a laser power of 95% and an exposure time of 900ms. Images were taken with a pixel size of 102nm and a total size of 1388x1040 pixels per tile scan. Subsequently, the sections were contrasted with 3% uranyl acetate and Reynold's lead citrate as described above. After checking the ultrastructure quality of the Centrin1-GFP positive cells on a Jeol JEM-1400 80 kV transmission electron microscope (Jeol) as described above, tomography was performed on a Tecnai F30 EM TEM (EMBL Heidelberg), operating at 300kV. Tilt series of 200 nm thick sections were recorded at the range of +-60° with 2° interval, on 4x4k CCD camera (Gatan - OneView), using Serial-EM acquisition software. 3D reconstructions and further analyses were conducted using "etomo" Image Processing Package (Boulders, Colorado). Correlation of fluorescence and electron tomography images was performed manually using Fiji, GIMP 2.10.20. and Inkscape.

530

531 **Transmission electron microscopy of Spurr-embedded infected RBCs**

532 For high pressure freezing of infected erythrocytes, a total of 1 ml packed red blood cells infected
533 with NF54 wild type parasites were grown in 35 ml culture medium. At a parasitemia of 6% late stage
534 parasites, schizonts were purified using magnetic separation (QuadroMACS™, Miltenyi Biotec).
535 Therefore, after equilibrating three LS columns with complete medium in the magnetic field, a flow
536 resistor (G23 needle, 0.6 mm diameter, BD Microlance) was attached to each. 6 ml of the parasite
537 culture were loaded onto each of the columns. After three washing steps with 3ml incomplete
538 medium each, the flow resistors were removed, the columns taken out of the magnetic field and late
539 stage parasites were eluted using 1ml complete medium each. The three eluates were pooled and 30
540 µl of uninfected packed red blood cells were added. The cells were cultured in 3 ml complete
541 medium for 4h to let them recover from the purification. For HPF, 6x 500 µl of the culture were
542 pelleted in individual 1.5 ml reaction tubes and temporarily stored at 37°C until high pressure
543 freezing of the sample using Leica EM ICE (Leica Microsystems). Briefly, gold carriers (3 mm diameter,
544 100 µm depth) and the respective lids were placed on hexadecane-soaked filter paper. The
545 supernatant was removed and a carrier (Leica Microsystems) was filled with around 1.5 µl of
546 concentrated schizont pellet, the lid was placed on top and the sample was high pressure frozen.
547 Freeze substitution was performed in an Automatic Freeze Substitution System (AFS2, Leica
548 Microsystems), with a freeze substitution solution containing 0.2% Osmium tetroxide, 0.3% uranyl
549 acetate, 5% H2O in dry acetone After incubation of the samples in the freeze substitution solution for
550 1h at -90°C, the temperature was increased from -90°C to +20°C in 22h (an increase of 5°C/h) and
551 stayed at 20°C until further processing. The freeze substitution solution was removed and washed
552 three times with dry acetone. The pellets detached from carriers and were combined for the next
553 steps. The combined pellets were transferred to a 1.5 ml reaction tube in dry acetone and pelleted
554 for 2min, 2200rpm. Acetone was replaced by a 1:1 mixture of Spurr's resin (Serva, Heidelberg) and
555 dry acetone. After a 2h incubation at room temperature, the 1:1 mixture was replaced by 100%
556 Spurr's resin and incubated over night at room temperature. The Spurrr's resin was removed and
557 again replaced by 100% Spurr's resin. Polymerization of the samples was performed at 60°C for 1-2
558 days. Samples were trimmed with a UC7 ultramicrotome (Leica Microsystems) and 70nm thin
559 sections were collected on Formvar-coated slot grids. Images were taken on a Jeol JEM-1400 80 kV
560 transmission electron microscope (Jeol) equipped with a 4k by 4k pixel TemCam F416 digital camera
561 (TVIPS). For image acquisition, the EM-Menu (TVIPS) software was used.

562

563 **Conflicts of Interest**

564

565 none declared

566

567 **Author Contributions**

568

569 Experiments were planned and designed by C.S.S with the help of J.G. Light microscopy and
570 immunofluorescence assays were carried out and analyzed by C.S.S. Electron microscopy was
571 realized by C.S.S with help by C.F. CLEM was realized by C.S.S with help by C.F, M.C and J.K.
572 PfCentrin1-GFP strains and the anti-PfCentrin3 antibody were produced by Y.V. NLS-mCherry and

Nup313-HA strains were generated by D.K, M.M and A.P with the help of M.G. J.G and C.S.S wrote the manuscript with comments by the other authors.

Funding

We thank the German Research Foundation (DFG) (349355339) and the Human Frontiers Science Program (CDA00013/2018-C) for funding to J.G and the "Studienstiftung des Deutschen Volkes" to Y.V. The German Research Foundation (DFG) – Project number 240245660 - SFB 1129 for funding to M.G and D.K and the Baden-Württemberg Foundation (1.16101.17) for funding to M.G, as well as the Fundação para a Ciência e Tecnologia (FCT, Portugal) - PD/BD/128002/2016 to M.M.

Acknowledgments

We thank: The Infectious Diseases Imaging Platform for imaging support (idip-heidelberg.org). The Electron Microscopy Core Facility (EMCF) at Heidelberg University for providing electron microscopy services. PlasmoDB for their *Plasmodium* Informatics Resources. Stefan Pitsch and Luc Reymond from Spirochrome LTD for providing their SPY555-Tubulin dye. Grazvydas Lukinavicius and Jonas Bucevicius from the Max Planck Institute for Biophysical Chemistry for providing the 5-SiR-Hoechst dye. Nicolas Lichti for help with molecular cloning. Marc-Jan Gubbels for the anti-TgCentrin1 and Alan Cowman for the anti-CenH3 antibodies.

References

Ader NR, Kukulski W. 2017. triCLEM: Combining high-precision, room temperature CLEM with cryo-fluorescence microscopy to identify very rare events. *Methods Cell Biol*. doi:10.1016/bs.mcb.2017.03.009

Aikawa M, Beaudoin R. 1968. Studies on Nuclear Division of a Malarial Parasite Under Pyrimethamine Treatment. *J Cell Biol* **39**:749–754. doi:10.1083/jcb.39.3.749

Aikawa M, Huff CG, Sprinz H. 1967. Fine structure of the asexual stages of Plasmodium elongatum. *J Cell Biol* **34**:229–249. doi:10.1083/jcb.34.1.229

Arnot DE, Ronander E, Bengtsson DC. 2011. The progression of the intra-erythrocytic cell cycle of Plasmodium falciparum and the role of the centriolar plaques in asynchronous mitotic division during schizogony. *Int J Parasitol* **41**:71–80. doi:10.1016/j.ijpara.2010.07.012

Azimzadeh J, Bornens M. 2007. Structure and duplication of the centrosome. *J Cell Sci* **120**:2139–2142. doi:10.1242/jcs.005231

Bannister LH, Hopkins JM, Fowler RE, Krishna S, Mitchell GH. 2000. Ultrastructure of rhoptry development in Plasmodium falciparum erythrocytic schizonts. *Parasitology* **121**:273–287. doi:10.1017/S0031182099006320

Beier JC. 1998. Malaria parasite development in mosquitoes. *Annu Rev Entomol* **43**:519–543. doi:10.1146/annurev.ento.43.1.519

Bertiaux E, Balestra A, Bournonville L, Brochet M, Guichard P, Hamel V. 2021. Expansion Microscopy provides new insights into the cytoskeleton of malaria parasites including the conservation of a conoid. *PLoS Biol* **19**. doi:10.1371/journal.pbio.3001020

Birnbaum J, Flemming S, Reichard N, Soares AB, Mesén-Ramírez P, Jonscher E, Bergmann B, Spielmann T. 2017. A genetic system to study Plasmodium falciparum protein function. *Nat Methods* **14**:450–456. doi:10.1038/nmeth.4223

Bucevičius J, Keller-Findeisen J, Gilat T, Hell SW, Lukinavičius G. 2019. Rhodamine-Hoechst positional isomers for highly efficient staining of heterochromatin. *Chem Sci* **12**:1962–1970. doi:10.1039/c8sc05082a

Canning EU, Sinden RE. 1973. The organization of the ookinete and observations on nuclear division in oocysts of Plasmodium berghei. *Parasitology* **67**:29–40. doi:10.1017/S0031182000046266

Dorin-Semblat D, Schmitt S, Semblat JP, Sicard A, Reininger L, Goldring D, Patterson S, Quashie N, Chakrabarti D, Meijer L, Doerig C. 2011. Plasmodium falciparum NIMA-related kinase Pfnek-1: Sex specificity and

624 assessment of essentiality for the erythrocytic asexual cycle. *Microbiology* **157**:2785–2794.
625 doi:10.1099/mic.0.049023-0
626 Fang H, Klages N, Baechler B, Hillner E, Yu L, Pardo M, Choudhary J, Brochet M. 2017. Multiple short windows
627 of calcium-dependent protein kinase 4 activity coordinate distinct cell cycle events during Plasmodium
628 gametogenesis. *Elife* **6**:1–23. doi:10.7554/eLife.26524
629 Fennell B, Naughton J, Dempsey E, Bell A. 2006. Cellular and molecular actions of dinitroaniline and
630 phosphorothioamidate herbicides on Plasmodium falciparum: Tubulin as a specific antimalarial target.
631 *Mol Biochem Parasitol* **145**:226–238. doi:10.1016/j.molbiopara.2005.08.020
632 Fennell BJ, Al-shatr ZA, Bell A. 2008. Isotype expression, post-translational modification and stage-dependent
633 production of tubulins in erythrocytic Plasmodium falciparum. *Int J Parasitol* **38**:527–539.
634 doi:10.1016/j.ijpara.2007.09.005
635 Francia ME, Striepen B. 2014. Cell division in apicomplexan parasites. *Nat Rev Microbiol* **12**:125–136.
636 doi:10.1038/nrmicro3184
637 Fu J, Hagan IM, Glover DM. 2015. The centrosome and its duplication cycle. *Cold Spring Harb Perspect Med*
638 **7**:a015800. doi:10.1101/cshperspect.a015800
639 Garg S, Agarwal S, Dabral S, Kumar N, Sehrawat S, Singh S. 2015. Visualization and quantification of
640 Plasmodium falciparum intraerythrocytic merozoites. *Syst Synth Biol* **9**:23–26. doi:10.1007/s11693-015-
641 9167-9
642 Gerald N, Mahajan B, Kumar S. 2011. Mitosis in the human malaria parasite plasmodium falciparum. *Eukaryot*
643 *Cell* **10**:474–482. doi:10.1128/EC.00314-10
644 Gibeaux R, Lang C, Politi AZ, Jaspersen SL, Philippsen P, Antony C. 2012. Electron tomography of the
645 microtubule cytoskeleton in multinucleated hyphae of Ashbya gossypii. *J Cell Sci* **125**:5830–9.
646 doi:10.1242/jcs.111005
647 Gruring C, Heiber A, Kruse F, Ungefehr J, Gilberger TW, Spielmann T. 2011. Development and host cell
648 modifications of Plasmodium falciparum blood stages in four dimensions. *Nat Commun* **2**:165.
649 doi:10.1038/ncomms1169
650 Gubbels MJ, Keroack CD, Dangoudoubiyam S, Worliczek HL, Paul AS, Bauwens C, Elsworth B, Engelberg K, Howe
651 DK, Coppens I, Duraisingh MT. 2020. Fussing About Fission: Defining Variety Among Mainstream and
652 Exotic Apicomplexan Cell Division Modes. *Front Cell Infect Microbiol* **5**:269.
653 doi:10.3389/fcimb.2020.00269
654 Guizetti J, Frischknecht F. 2021. Apicomplexans: A conoid ring unites them all. *PLoS Biol* **19**:e3001105.
655 doi:10.1371/journal.pbio.3001105
656 Heald R, Khodjakov A. 2015. Thirty years of search and capture: The complex simplicity of mitotic spindle
657 assembly. *J Cell Biol*. doi:10.1083/jcb.201510015
658 Hoeijmakers WAM, Flueck C, Françoijs KJ, Smits AH, Wetzel J, Volz JC, Cowman AF, Voss T, Stunnenberg HG,
659 Bártfai R, Francoijs KJ, Smits AH, Wetzel J, Volz JC, Cowman AF, Voss T, Stunnenberg HG, Bartfai R. 2012.
660 Plasmodium falciparum centromeres display a unique epigenetic makeup and cluster prior to and during
661 schizogony. *Cell Microbiol* **14**:1391–1401. doi:10.1111/j.1462-5822.2012.01803.x
662 Höög JL, Schwartz C, Noon AT, O'Toole ET, Mastronarde DN, McIntosh JR, Antony C. 2007. Organization of
663 Interphase Microtubules in Fission Yeast Analyzed by Electron Tomography. *Dev Cell* **12**:349–61.
664 doi:10.1016/j.devcel.2007.01.020
665 Howells RE, Davies EE. 1971. Nuclear division in the oocyst of Plasmodium berghei. *Ann Trop Med Parasitol*
666 **65**:451–9. doi:10.1080/00034983.1971.11686777
667 Kehrer J, Kuss C, Andres-Pons A, Reustle A, Dahan N, Devos D, Kudryashev M, Beck M, Mair GR, Frischknecht F.
668 2018. Nuclear Pore Complex Components in the Malaria Parasite Plasmodium berghei. *Sci Rep* **26**:11249.
669 doi:10.1038/s41598-018-29590-5
670 Kilmartin J V. 2014. Lessons from yeast: The spindle pole body and the centrosome. *Philos Trans R Soc B Biol Sci*
671 **369**:20130456. doi:10.1098/rstb.2013.0456
672 Kremer JR, Mastronarde DN, McIntosh JR. 1996. Computer visualization of three-dimensional image data using
673 IMOD. *J Struct Biol* **116**:71–76. doi:10.1006/jsbi.1996.0013
674 Kukulski W, Schorb M, Welsch S, Picco A, Kaksonen M, Briggs JAG. 2012. Precise, Correlated Fluorescence
675 Microscopy and Electron Tomography of Lowicryl Sections Using Fluorescent Fiducial MarkersMethods in
676 Cell Biology. doi:10.1016/B978-0-12-416026-2.00013-3
677 Kukulski W, Schorb M, Welsch S, Picco A, Kaksonen M, Briggs JAG. 2011. Correlated fluorescence and 3D
678 electron microscopy with high sensitivity and spatial precision. *J Cell Biol*. doi:10.1083/jcb.201009037
679 Leete TH, Rubin H. 1996. Malaria and the cell cycle. *Parasitol Today* **12**:442–444. doi:10.1016/0169-
680 4758(96)10068-5
681 Lutz R, Bujard H. 1997. Independent and tight regulation of transcriptional units in escherichia coli via the

682 LacR/O, the TetR/O and AraC/I1-I2 regulatory elements. *Nucleic Acids Res* **25**:1203–10.
683 doi:10.1093/nar/25.6.1203
684 Mahajan B, Selvapandiyan A, Gerald NJ, Majam V, Zheng H, Wickramarachchi T, Tiwari J, Fujioka H, Moch JK,
685 Kumar N, Aravind L, Nakhasi HL, Kumar S. 2008. Centrins, cell cycle regulation proteins in human malaria
686 parasite Plasmodium falciparum. *J Biol Chem* **283**:31871–31883. doi:10.1074/jbc.M800028200
687 Mastronarde DN. 2005. Automated electron microscope tomography using robust prediction of specimen
688 movements. *J Struct Biol* **152**:36–51. doi:10.1016/j.jsb.2005.07.007
689 Matthews H, Duffy CW, Merrick CJ. 2018. Checks and balances? DNA replication and the cell cycle in
690 Plasmodium. *Parasites and Vectors* **11**:216. doi:10.1186/s13071-018-2800-1
691 Mehnert AK, Simon CS, Guizetti J. 2019. Immunofluorescence staining protocol for STED nanoscopy of
692 Plasmodium-infected red blood cells. *Mol Biochem Parasitol* 47–52.
693 doi:10.1016/j.molbiopara.2019.02.007
694 O'Toole ET, McDonald KL, Mäntler J, McIntosh JR, Hyman AA, Müdler-Reichert T. 2003. Morphologically distinct
695 microtubule ends in the mitotic centrosome of Caenorhabditis elegans. *J Cell Biol* **163**:451–6.
696 doi:10.1083/jcb.200304035
697 Prensier G, Slomianny C. 1986. The karyotype of Plasmodium falciparum determined by ultrastructural serial
698 sectioning and 3D reconstruction. *J Parasitol* **72**:731–736.
699 Press A. 2018. The Karyotype of Plasmodium falciparum Determined by Ultrastructural Serial Sectioning and 3D
700 Reconstruction Author (s): G . Prensier and Ch . Slomianny Source : The Journal of Parasitology , Vol . 72
701 , No . 5 (Oct ., 1986), pp . 731-736 Published by **72**:731–736.
702 Prudêncio M, Rodriguez A, Mota MM. 2006. The silent path to thousands of merozoites: The Plasmodium liver
703 stage. *Nat Rev Microbiol* **4**:849–856. doi:10.1038/nrmicro1529
704 Read M, Sherwin T, Holloway SP, Gull K, Hyde JE. 1993. Microtubular organization visualized by
705 immunofluorescence microscopy during erythrocytic schizogony in Plasmodium falciparum and
706 investigation of post-translational modifications of parasite tubulin. *Parasitology* **106**:223–232.
707 doi:10.1017/S0031182000075041
708 Reilly HB, Wang H, Steuter JA, Marx AM, Ferdig MT. 2007. Quantitative dissection of clone-specific growth rates
709 in cultured malaria parasites. *Int J Parasitol* **37**:1599–1607. doi:10.1016/j.ijpara.2007.05.003
710 Richmond D, Rizkallah R, Liang F, Hurt MM, Wang Y. 2013. Slk19 clusters kinetochores and facilitates
711 chromosome bipolar attachment. *Mol Biol Cell* **24**:566–77. doi:10.1091/mbc.E12-07-0552
712 Roques M, Stanway RR, Rea EI, Markus R, Brady D, Holder AA, Guttery DS, Tewari R. 2019. Plasmodium centrin
713 Pb CEN-4 localizes to the putative MTOC and is dispensable for malaria parasite proliferation. *Biol Open*
714 **8**:bio036822. doi:10.1242/bio.036822
715 Rüthnick D, Schiebel E. 2018. Duplication and Nuclear Envelope Insertion of the Yeast Microtubule Organizing
716 Centre, the Spindle Pole Body. *Cells* **7**:42. doi:10.3390/cells7050042
717 Schindelin J, Arganda-Carreras I, Frise E, Kaynig V, Longair M, Pietzsch T, Preibisch S, Rueden C, Saalfeld S,
718 Schmid B, Tinevez JY, White DJ, Hartenstein V, Eliceiri K, Tomancak P, Cardona A. 2012. Fiji: An open-
719 source platform for biological-image analysis. *Nat Methods* **9**:676–682. doi:10.1038/nmeth.2019
720 Schofield L. 2007. Intravascular infiltrates and organ-specific inflammation in malaria pathogenesis. *Immunol*
721 *Cell Biol* **85**:130–137. doi:10.1038/sj.icb.7100040
722 Schrével J, Asfaux-Foucher G, Bafort JM. 1977. Etude ultrastructurale des mitoses multiples au cours de la
723 sporogonie du Plasmodium b. berghei. *J Ultrasructure Res* **59**:332–50. doi:10.1016/S0022-
724 5320(77)90043-0
725 Sinden RE, Canning EU, Bray RS, Smalley ME. 1978. Gametocyte and gamete development in Plasmodium
726 falciparum. *Proc R Soc London - Biol Sci* **201**:375–99. doi:10.1098/rspb.1978.0051
727 Sinden RE, Canning EU, Spain B. 1976. Gametogenesis and fertilization in Plasmodium yoelii nigeriensis: a
728 transmission electron microscope study. *Proc R Soc London Ser B, Biol Sci* **193**:55—76.
729 doi:10.1098/rspb.1976.0031
730 Sturm A, Amino R, Van De Sand C, Regen T, Retzlaff S, Rennenberg A, Krueger A, Pollok JM, Menard R, Heussler
731 VT. 2006. Manipulation of host hepatocytes by the malaria parasite for delivery into liver sinusoids.
732 *Science (80-)* **313**:1287–1290. doi:10.1126/science.1129720
733 Suvorova ES, Francia M, Striepen B, White MW. 2015. A Novel Bipartite Centrosome Coordinates the
734 Apicomplexan Cell Cycle. *PLoS Biol* **13**:1–29. doi:10.1371/journal.pbio.1002093
735 Terzakis JA, Sprinz H, Ward RA. 1967. The transformation of the Plasmodium gallinaceum oocyst in Aedes
736 aegypti mosquitoes. *J Cell Biol* **34**:311–326. doi:10.1083/jcb.34.1.311
737 Vaughan JA. 2007. Population dynamics of Plasmodium sporogony. *Trends Parasitol* **23**:63–70.
738 doi:10.1016/j.pt.2006.12.009
739 Volz J, Carvalho TG, Ralph SA, Gilson P, Thompson J, Tonkin CJ, Langer C, Crabb BS, Cowman AF. 2010. Potential

740 epigenetic regulatory proteins localise to distinct nuclear sub-compartments in Plasmodium falciparum.
741 *Int J Parasitol* **40**:109–121. doi:S0020-7519(09)00367-1 [pii] 10.1016/j.ijpara.2009.09.002
742 Walker RA, O'Brien ET, Pryer NK, Soboeiro MF, Voter WA, Erickson HP, Salmon ED. 1988. Dynamic instability of
743 individual microtubules analyzed by video light microscopy: rate constants and transition frequencies. *J*
744 *Cell Biol* **107**:1437–48. doi:10.1083/jcb.107.4.1437
745 Wang L, Tran M, D'Este E, Roberti J, Koch B, Xue L, Johnsson K. 2020. A general strategy to develop cell
746 permeable and fluorogenic probes for multicolour nanoscopy. *Nat Chem* **12**:165–72. doi:10.1038/s41557-
747 019-0371-1
748 White MW, Suvorova ES. 2018. Apicomplexa Cell Cycles: Something Old, Borrowed, Lost, and New. *Trends*
749 *Parasitol* **34**:759–71. doi:10.1016/j.pt.2018.07.006
750 Woodruff JB, Wueseke O, Hyman AA. 2014. Pericentriolar material structure and dynamics. *Philos Trans R Soc*
751 *Lond B Biol Sci* **369**:20130459-. doi:10.1098/rstb.2013.0459
752 Zeeshan M, Pandey R, Ferguson DJP, Tromer EC, Markus R, Abel S, Brady D, Daniel E, Limenitakis R, Bottrill AR,
753 Le Roch KG, Holder AA, Waller RF, Guttery DS, Tewari R. 2020. Real-time dynamics of Plasmodium NDC80
754 reveals unusual modes of chromosome segregation during parasite proliferation. *J Cell Sci* **134**:jcs245753.
755 doi:10.1242/JCS.245753
756 Zupa E, Liu P, Würtz M, Schiebel E, Pfeffer S. 2020. The structure of the γ-TuRC: a 25-years-old molecular
757 puzzle. *Curr Opin Struct Biol* 15–21. doi:10.1016/j.sbi.2020.08.008
758